RESEARCH ARTICLE

**CARBON ENERGY** WILEY

# Effects of nanopores and sulfur doping on hierarchically bunched carbon fibers to protect lithium metal anode

Ji In Jung[1] | Sunwoo Park[1] | Son Ha[2] | Se Youn Cho[3] | Hyoung-Joon Jin[1,4] | Young Soo Yun[2,5] (ORCID)

[1]Program in Environmental and Polymer Engineering, Inha University, Incheon, South Korea

[2]KU-KIST Graduate School of Converging Science and Technology, Korea University, Seoul, South Korea

[3]Carbon Composite Materials Research Center, Korea Institute of Science and Technology, Wanju-gun, Jeollabuk-do, South Korea

[4]Department of Polymer Science and Engineering, Inha University, Incheon, South Korea

[5]Department of Integrative Energy Engineering, Korea University, Seoul, South Korea

**Correspondence**
Hyoung-Joon Jin, Program in Environmental and Polymer Engineering, Inha University, 100, Inha-ro, Michuhol-gu, Incheon 22212, South Korea.
Email: hjjin@inha.ac.kr

Young Soo Yun, KU-KIST Graduate School of Converging Science and Technology, Korea University, 145, Anam-ro, Seongbuk-gu, Seoul 02841, South Korea.
Email: c-ysyun@korea.ac.kr

**Funding information**
National Research Foundation of Korea, Grant/Award Numbers: 2019R1A2C1084836, 2021R1A4A2001403

**Abstract**

Studies on three-dimensional structured carbon templates have focused on how to guide homogeneous lithium metal nucleation and growth for lithium metal anodes (LMAs). However, there is still insufficient evidence for a key factor to achieve their high electrochemical performance. Here, the effects of nanopores and sulfur doping on carbon-based nanoporous host (CNH) electrode materials for LMAs were investigated using natural polymer-derived CNHs. Homogeneous pore-filling behaviors of lithium metal in the nanopores of the CNH electrode materials were first observed by ex situ scanning electron microscopy analysis, where the protective lithium metal nucleation and growth process led to significantly high Coulombic efficiency (CE) of ~99.4% and stable 600 cycles. In addition, a comparison study of CNH and sulfur-doped CNH (S-CNH) electrodes, which differ only in the presence or absence of sulfur, revealed that sulfur doping can cause lower electrochemical series resistance, higher CE value, and better cycling stability in a wide range of current densities and number of cycles. Moreover, S-CNH-based LMAs showed high electrochemical performance in full-cell Li–S battery tests using a sulfur copolymer cathode, where a high energy density of $1370\,W\,h\,kg_{electrode}^{-1}$ and an excellent power density of $4120\,W\,kg_{electrode}^{-1}$ were obtained.

**KEYWORDS**
carbon template, Li–S batteries, lithium metal anode, lithium metal batteries, nanoporous carbon, sulfur doping

# 1 | INTRODUCTION

Lithium metal anodes (LMAs) have attracted considerable research interest for use in rechargeable lithium batteries (RLBs) due to their high energy performance (specific capacity: ~3860 mAh g$^{-1}$, redox voltage: −3.04 V vs. standard hydrogen electrode) and high power capability.[1,2] However, LMAs have poor Coulombic efficiency (CE) and low cycling stability owing to (1) the infinite volume change accompanying continuous side reactions, (2) a decrease in the corrosive active surfaces by the accumulation of inactive byproducts, and (3) unexpected cell death due to electrode short circuits induced by metal dendrite growth.[3–4] To address these issues, LMAs were initially applied using a large amount of excessive lithium metal and electrolyte solution to replace lithium and solvent lost during cycling, respectively[5,6] These LMAs exhibited good cycle life, but the use of excess lithium and electrolyte significantly decreased the specific/volumetric energy density of RLBs and posed potentially fatal safety hazards.[7] Therefore, studies on how to establish a feasible LMA system have focused on minimizing the excess use of lithium metal in LMAs through sophisticated electrode design and electrolyte engineering.[8–11] Among several research approaches, 3D-structured carbon-based electrode materials with high active surface areas have been shown to guide homogeneous metal deposition/dissolution cycles with high CE, where the more highly functionalized carbons can provide more active surfaces for metal nucleation and growth.[12–19] The large number of nucleation sites can significantly decrease the overpotential, resulting in simultaneous growth of lithium metal on all the surfaces.[20,21] However, the functionalized carbon surface is prone to degradation and is converted to inactive byproducts during cycling, which results in poor cycling performance.[22–24] Therefore, it is necessary to introduce more rigid and effective functional groups that guide catalytic lithium metal deposition to obtain better cycling performance of three-dimensional (3D) carbonaceous electrode materials. More importantly, lithium metal growth on the 3D open surface results in continuous side reactions that produce byproducts, even when highly efficient catalytic electrode materials and electrolyte systems are used.[21] The infinite volume changes during the growth of lithium metal inevitably cause severe damage to the solid electrolyte interface (SEI) layer that covers the metal; consequently, the SEI layer must be renewed by side reactions with the electrolyte solution.[25,26] Therefore, developing a nanoporous template for the growth of protective lithium metal can be a better strategy to improve the CE and solve the safety problem.

Here, we report a functionalized carbon-based nanoporous host (CNH) strategy for protecting LMAs.

Functionalized carbons were fabricated from traditional Korean paper handmade from mulberry trees by a high-temperature heating process, because mulberry paper (MP) has a unique microcrystalline structure that can be transformed into nanoporous carbonaceous structure by simple pyrolysis. The MP-based CNHs were further thermally treated with elemental sulfur to introduce sulfur into the defective carbon structure. The resulting sulfur-doped CNHs (S-CNHs) have a distinctive fibrous morphology composed of hierarchically bunched nanofibrils with a high specific surface area of ~340 m$^2$ g$^{-1}$, nanopores in a broad size range of 1–100 nm, and lithiophilic chalcogen functional groups (O/C and S/C ratios of 0.13 and 0.05, respectively). To investigate the effects of sulfur doping on the carbon-based host electrode materials, the electrochemical performance of CNHs and S-CNHs, which are similar except for the presence or absence of sulfur, was compared. In addition, ex situ field emission scanning electron microscopy (FE-SEM) observation was performed to reveal the effect of nanopores on the reversible lithium metal storage behavior. These observations demonstrated experimentally the strong effects of sulfur doping and nanopores on the CNH electrodes.

# 2 | EXPERIMENTAL SECTION

## 2.1 | Preparation of CNH and S-CNH electrodes

CNHs were prepared from mulberry-tree-derived commercial MP (Cheongsong Hanji). The MP was thermally treated in a tube furnace at 180°C for 6 h under N$_2$ flow at 200 mL min$^{-1}$. Next, it was heated to 800°C at a rate of 10°C min$^{-1}$ and held at 800°C for 2 h. The tube furnace was then naturally cooled to room temperature, and the obtained CNH was washed several times with ethanol and distilled water. The S-CNH was prepared by the same procedure except for the addition of elemental sulfur. Approximately 10 wt% of elemental sulfur (Sigma-Aldrich) with respect to the MP was introduced during heating. Electrodes, a half-inch in diameter, were obtained by punching the as-prepared CNH and S-CNH materials and used as the electrodes for LMA in symmetric cells and full-cell systems.

## 2.2 | Preparation of S-DIB cathode

Elemental sulfur (8 g) was heated to 185°C in a 30-mL vial under mild stirring. When it melted to an orange liquid, 2 g of 1,3-diisopropenylbenzene (DIB) (Tokyo

Chemical Industry Co., Ltd.) was injected into the vial for an inverse vulcanization reaction. After 4 min, the polymerization reaction of sulfur and DIB was terminated by the high viscosity. To remove the unreacted DIB, the polymerized sulfur copolymer [poly(sulfur-*random*-1, 3-diisopropenylbenzene)] was heated at 185°C for 10 min in a vacuum oven. It was then cooled to room temperature and ground to a powder in liquid nitrogen. The as-prepared S-DIB was composed of 80 wt% sulfur and 20 wt% DIB. To prepare the S-DIB cathode, the S-DIB powder was mixed with conductive carbon and a polyvinylidene fluoride (Sigma-Aldrich) binder at a weight ratio of 6:3:1 in a mortar with an N-methyl -2-pyrrolidone solution. The slurry was coated on Al foil and dried in a vacuum oven at 80°C for 12 h. A half-inch-diameter cathode was punched from the as-prepared S-DIB material and used in the full-cell systems.

## 2.3 | Characterization

The bare and ex situ morphologies of CNHs and S-CNHs were observed by FE-SEM (S-4300SE; Hitachi). Field emission transmission electron microscopy (JEM2100F; JEOL) was used to analyze the carbon microstructure of the CNHs and S-CNHs. For the X-ray diffreaction (XRD) analysis (DMAX 2500; Rigaku), a Cu Kα radiation ($\lambda = 0.154$ nm) generator was used in a 2θ range of 5°–60° at 100 mA and 40 kV. Raman spectroscopy (LabRAM HR Evolution; Horiba) was conducted using a laser (wavelength: 514.5 nm), a 1200 groove mm$^{-1}$ grating, and a ×1000 objective lens. The laser spot diameter was ~1 nm. X-ray photoelectron spectroscopy (XPS) (PHI 5700 ESCA) was performed using monochromatic Al Kα radiation for surface analysis and ex situ depth profile analysis with an etching time of 100 s. The specific surface area and porosity of the CNHs and S-CNHs were characterized using nitrogen adsorption/desorption isotherms (ASAP 2020; Micromeritics). Electrical conductivities of the CNHs and S-CNHs were measured by an electrical conductivity meter (Loresta GP; Mitsubishi Chemical).

## 2.4 | Electrochemical characterization

The electrochemical performance of bare Cu foil, CNH, S-CNH, and S-DIB half cells and full cells were tested using an automatic battery cycler (WonATech) and coin cells (CR2032 type). The coin cells were assembled in a glove box filled with high-purity argon gas for half-cell tests with Cu foil, CNH, S-CNH, or S-DIB as the working electrode and Li foil as both the reference and counter

electrodes. An electrolyte was prepared by dissolving 1 M LiTFSI (>99.95%; Aldrich) in a DOL/DME (1:1 volume/volume) mixture solution containing 2 wt% LiNO$_3$ and used in all the electrochemical tests. A glass microfiber filter was used as a separator (GF/F; Whatman). For the electrochemical impedance spectroscopy (EIS) analyses, the half cells were tested in a frequency range of 1 mHz to 0.1 MHz using an impedance analyzer (ZIVE SP2; WonATech). For the full-cell tests, a precycled S-CNH-based LMA including 5 mAh cm$^{-2}$ of Li metal was assembled with an S-DIB cathode in a coin cell and the electrochemical performance was characterized by galvanostatic methods at different current densities.

## 3 | RESULTS AND DISCUSSION

The precursor, MP, has a well-developed macroporous network structure composed of randomly oriented microfibers and hierarchically assembled nanofibril bundles (Figure S1). The MP is subjected to a pyrolysis at 800°C, followed by heating with elemental sulfur; SEM images show that their distinctive 3D morphology is well maintained during heating treatment (Figures 1A,B and S2). In contrast, the nanofibrils comprising the microfibers are flattened and more densely packed during the thermal transition, because the cellulose-based polymer backbones are thermally transformed into basic structural units (BSUs) of pseudo-2D-structured carbon (Figure 1C). The material properties of the carbon BSUs in the CNHs and S-CNHs were characterized by their XRD patterns and Raman spectra (Figures 1D,E). In the XRD patterns, very broad graphite (002) peaks appeared; the R values were only 1.12 and 1.13 for CNHs and S–CNHs, respectively (Figure 1D). The very low R values close to 1 indicate that the BSUs are poorly stacked and most of them are present as single layers.[27] The signature D and G bands in the Raman spectra also reveal that both the CNHs and S–CNHs have an amorphous carbon structure composed of defective BSUs (Figure 1E). The D-to-G intensity ratios of the CNHs and S-CNHs are similar (1.46 and 1.47, respectively), indicating that they are composed of BSUs with crystalline planes approximately 3 nm in size (Figure S3).[28,29] These results reveal that the microstructure of the CNHs was slightly affected by heating with elemental sulfur.

The porous properties of the carbonaceous templates were investigated by nitrogen adsorption/desorption isotherm analysis (Figure 1F). The isotherm curves show unique adsorption and desorption shapes that have not been defined by the International Union of Pure and Applied Chemistry. The initial sharp increase in nitrogen adsorption volume originates from monolayer adsorption on the open surfaces and indicates that many micropores
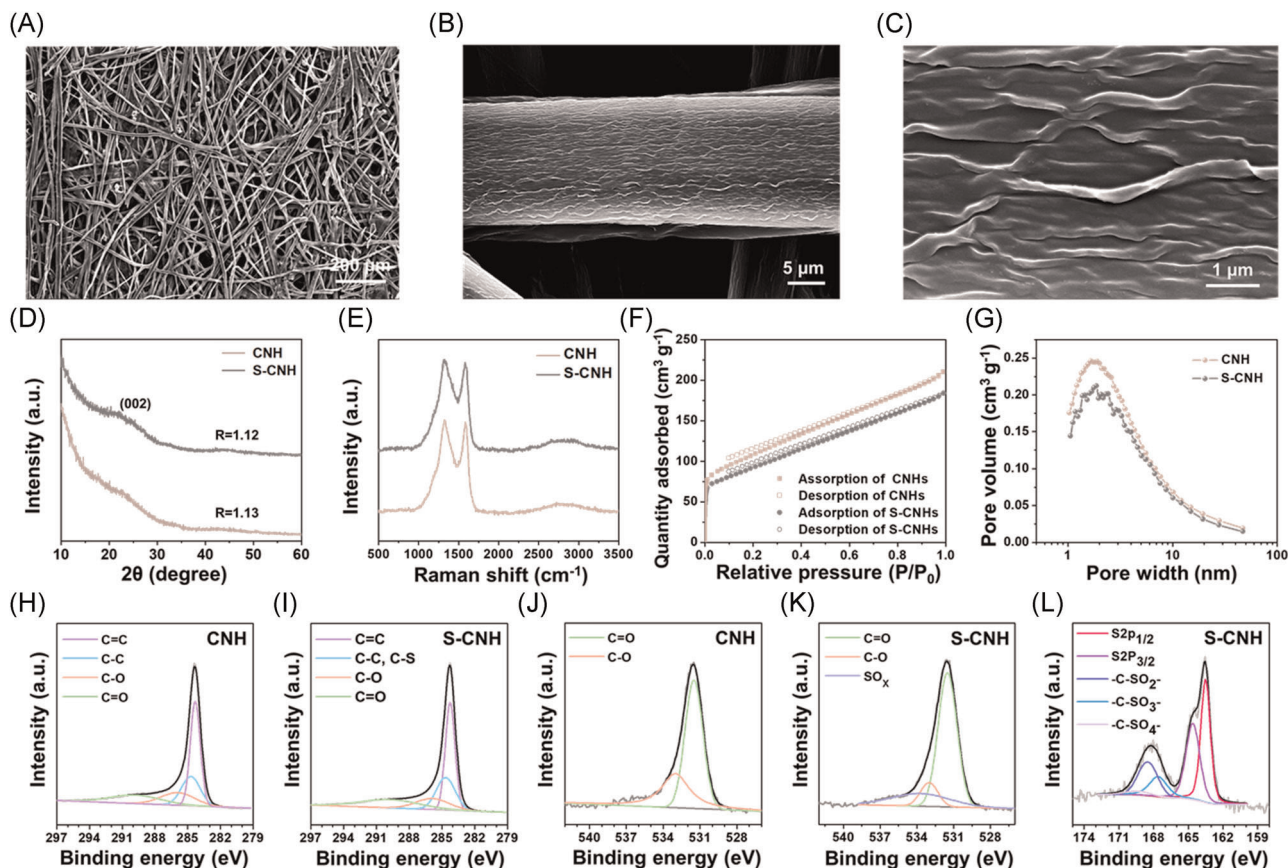
**FIGURE 1** Materials properties of CNHs and S-CNHs. (A–C) FE-SEM images of S-CNHs at different magnifications; (D) XRD patterns, (E) Raman spectra, (F) nitrogen adsorption and desorption isotherm curves, and (G) pore size distribution data of CNHs and S-CNHs; XPS C 1s spectra of (H) CNHs and (I) S-CNHs, O 1s spectra of (J) CNHs and (K) S-CNHs, and (L) S 2p spectrum of S-CNHs. CNH, carbon-based nanoporous host; FE-SEM, field emission scanning electron microscopy; S-CNH, sulfur-doped carbon-based nanoporous host; XPS, X-ray photoelectron spectroscopy; XRD, X-ray diffreaction

(<2 nm) are present. The isotherm curves exhibit a linear increase owing to atmospheric pressure, and no hysteresis appears between the adsorption and desorption curves. The isotherm curve differs from that of typical pore-filling behavior on mesopores showing the hysteresis by intermolecular interactions among neighboring nitrogen atoms. Due to the large amount of nitrogen adsorption and lack of hysteresis, the linear increase section is attributed to few-layer adsorption on small mesopores that are close to the micropore region (~2 nm). Pore size distribution data support this conclusion. Most of the pores range broadly in size between 1 and 100 nm, with a peak pore width of ~2 nm (Figure 1G). The specific Brunauer–Emmett–Teller surface areas of the CNHs and S-CNHs are ~370 and ~340 m$^2$ g$^{-1}$, respectively. Sulfur doping decreases the specific surface area slightly; however, the pore shape and distribution are well maintained.

The surface chemical properties of the CNHs and S-CNHs were analyzed by XPS. In the C 1s spectra, aromatic carbon–carbon double bonds centered at

~284.4 eV were detected as the primary carbon structure (Figures 1H,I). In addition, sp$^3$-hybridized carbon–carbon single bonds and carbon–oxygen single and double bonds were observed at ~284.7, ~286.0, and ~289.8 eV, respectively (Figures 1H,I).[30] The carbon–sulfur bonds were not clearly detected because their binding energy is similar to that of sp$^3$ C–C bonding. The C–O and C=O configurations also appeared in the O 1s spectra of both samples (Figures 1J,K). The oxygen heteroatoms cause the carbonaceous electrode to become electrolytephilic, increasing the electrochemically active surface area owing to good wettability with an organic electrolyte. In addition, the oxygen functional groups are known to be redox centers for lithium ions, where the highly electronegative oxygen binds strongly with lithium ions, which can facilitate lithium metal nucleation by reducing the surface tension.[31] In addition, the O 1s spectrum of the S-CNHs shows the presence of sulfate groups such as S–O$_x$ at 534.2 eV. The S 2p spectrum of the S-CNHs more clearly reveals sulfate bonding configurations such as C–SO$_2$, C–SO$_3$, and C–SO$_4$

(Figure 1L). Previously reported results revealed that sulfur oxide groups have a catalytic effect for lithium metal nucleation, where the lithiophilic functional groups guided homogeneous lithium metal growth on carbonaceous substrates, resulting in a high CE and stable cycling behavior.[32] In addition, the S 2p spectrum of the S-CNHs shows C–S–C and C=S bonds at 163.5 and 164.6 eV, respectively (Figure 1L). Carbon–sulfur bonds form primarily in defective carbon structure, which can be stabilized by sulfur, mitigating the degradation of the carbon structure during repeated lithium metal deposition/dissolution cycles.[33] In addition, the high chalcogen doping has n-type doping effects, resulting in a large increase in electrical conductivity.[33,34] Electrical conductivities of the CNHs and S-CNHs were characterized by a four-probe method, where the S-CNHs revealed a four times higher electrical conductivity corresponding to $\sim 8.4 \times 10^1 \, S \, cm^{-1}$ than that $(\sim 2.0 \times 10^1 \, S \, cm^{-1})$ of the CNHs. Thus, the positive effects of chalcogen doping can improve the electrochemical performance of S-CNHs, in particular the lithium metal nucleation and growth behavior in LMAs. The O/C ratios of the CNHs and S-CNHs are 0.14 and 0.13, respectively, and the S/C ratio of the S-CNHs is 0.05. As sulfur oxide groups contain multiple oxygen bonds, the many oxygen functional groups on the CNHs could be transformed into the sulfur oxide configuration during heating with elemental sulfur. However, the S-CNHs have large numbers of oxygen functional groups, in addition to the sulfur oxide and carbon sulfide functional groups (Figures 1H–L). The synergistic effects of the chalcogen-based functional groups resulted in superb electrochemical performance of the LMAs, as shown in the following section.

The electrochemical performance of the S-CNH electrodes for lithium metal deposition/dissolution was characterized using 1 M LiTFSI in 1,3-dioxolane (DOL)/dimethyl ether (DME) with 2 wt% LiNO₃ as an electrolyte, with a cut-off capacity of 5.0 mAh cm⁻² at different areal current rates. The results were compared with those of CNH electrodes to demonstrate the effects of sulfur doping (Figure 2). First of all, we conducted cyclic voltammetry (CV) tests for the S-CNH and CNH electrodes and a reference super P electrode in a voltage window between 0.01 and 2.5 V versus Li⁺/Li, to compare their electrochemically active surface areas (Figure S4). The first CV curve of the super P electrode shows larger reduction peaks and reduction curve areas than that of the CNH and S-CNH electrodes (Figure S4a). The reduction peak at ~1.6 V results from a decomposition of LiNO₃ additive, and the following broad peaks observed below 1.5 V originate from SEI formation reactions. The larger reduction peaks and curve areas indicate that an active surface area of the super P electrode is larger than that of

CNH and S-CNH electrodes. It should be noted that the super P has much lower BET specific surface area (72.3 m² g⁻¹) than that of the S-CNHs and CNHs (~340 and ~370 m² g⁻¹, respectively) (Figure S5). Despite the lower specific surface area, the super P electrode shows larger reduction peaks and curve areas. This means that the bulk fiber surfaces/near surfaces of S–CNHs and CNHs are covered by SEI layers, whereas their interior nanopores are closed for the solvent molecules. Nevertheless, the second and third curve areas of the S-CNH and CNH electrodes are larger than that of the super P electrode, indicating more reversible lithium ion storage capacities of the S-CNH and CNH electrodes (Figure S4b–d). Hence, S-CNHs and CNHs can induce protective lithium metal nucleation/dissolution cycles in the closed nanopores, and thereby high Coulombic efficiencies and cycling stabilities can be achieved.

The first galvanostatic lithium metal deposition profiles of S-CNH, CNH, and bare Cu foil electrodes show a voltage overshoot effect originating from the lithium metal nucleation overpotential (LMNO; Figure 2A). As shown in Figure S6, the LMNO is defined as the difference between the activation energy of the lithium metal reduction reaction and the formation energy gap between the metal and ions. The S-CNH, CNH, and bare Cu foil electrodes show large differences in LMNO, for example, values of 6.0, 8.4, and 19.6 mV, respectively, at the same areal current density. This result indicates that the sulfur oxide groups exhibit more effective catalytic performance for lithium metal nucleation than oxygen heteroatoms, because the other material properties of S-CNH and CNH electrodes are similar. In addition, S-CNH and CNH electrodes reveal stable lithium metal deposition/dissolution profiles at current rates ranging from 0.2 to 6.0 mA cm⁻², indicating good rate capability (Figures 2B,C). In the EIS profiles, the 1st cycles of both electrodes show two small semicircles corresponding to the surface film resistance ($R_f$) and charge-transfer resistance ($R_{ct}$), indicating that highly ion-conductive SEI layers were formed and successive lithium metal plating reactions occurred efficiently (Figures 2D,E). The small initial $R_f$ and $R_{ct}$ values of the S-CNH electrode (~10 and ~6 Ω, respectively) were well maintained after 50 cycles, indicating good stability of the SEI layer and high reversibility of the lithium metal storage behavior (Figure 2D). By contrast, the $R_f$ and $R_{ct}$ values of the CNH electrode increased after 50 cycles, from ~12 to ~20 Ω and from ~6 to ~17 Ω, respectively, implying poor cycling stability (Figure 2E).

The average CE of the CNHs and S-CNHs for 100 cycles (between the 10th and 110th cycles) was characterized at different areal current densities using more than 10 cells for each current density to increase the
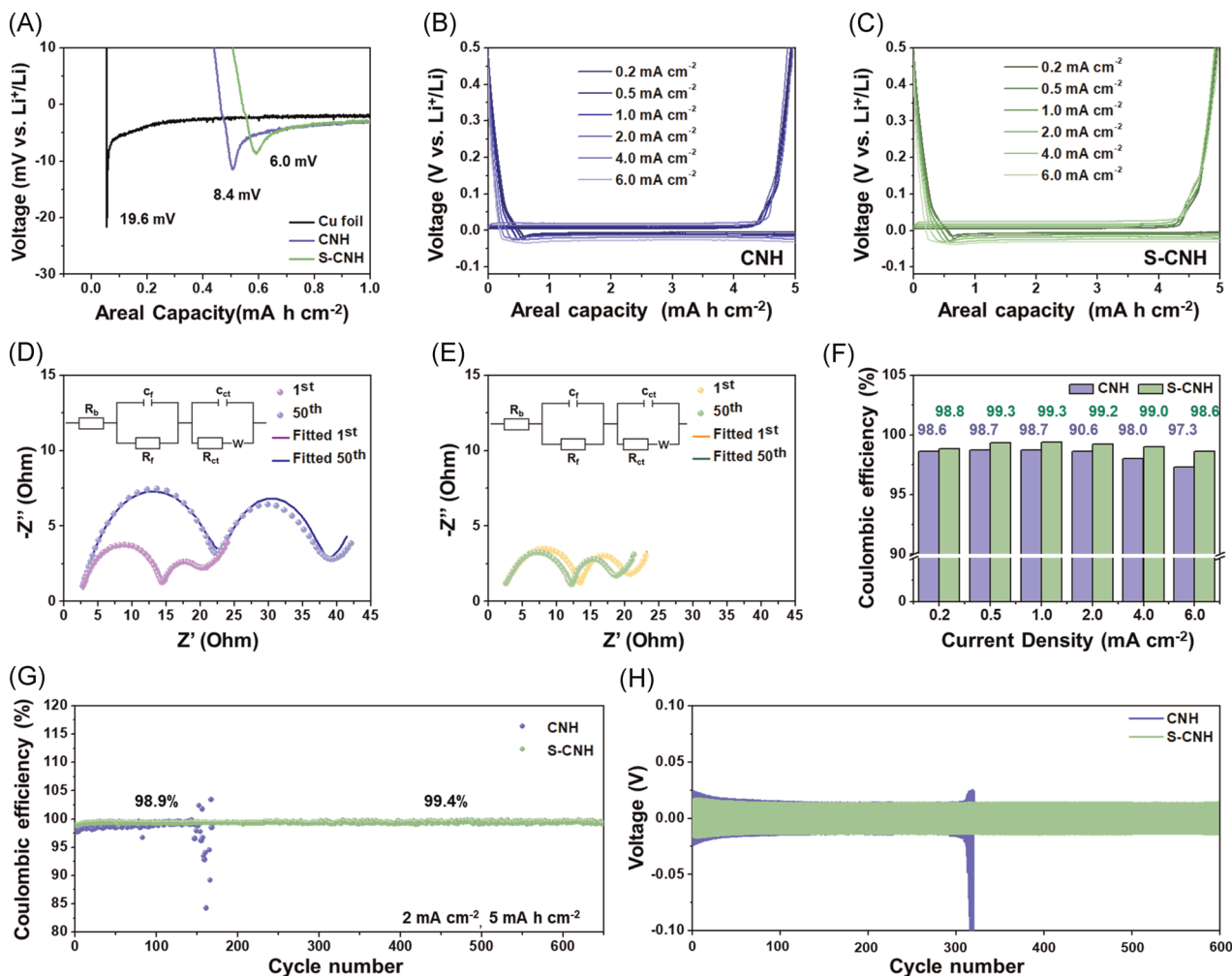
**FIGURE 2** Electrochemical performance of CNH and S-CNH electrodes. (A) Galvanostatic discharge profiles including a reference profile of a bare Cu foil electrode at $50\,\mu A\,cm^{-2}$; galvanostatic lithium metal deposition/dissolution profiles of (B) CNH and (C) S-CNH electrodes at different areal current rates; EIS profiles of (D) CNH and (E) S-CNH electrodes after 1st and 50th cycles; (F) bar graph of average CE at different areal current rates; (G) cycling performance at a cut-off capacity of $5\,mAh\,cm^{-2}$ and an areal current rate of $2\,mA\,cm^{-2}$; (H) cycling performance of symmetric cells with Li/CNH//Li/CNH and Li/S-CNH//Li/S-CNH configurations, which include lithium metal, $5\,mAh\,cm^{-2}$. CE, Coulombic efficiency; CNH, carbon-based nanoporous host; EIS, electrochemical impedance spectroscopy; S-CNH, sulfur-doped carbon-based nanoporous host

reliability (Figure 2F). For the CNHs, a maximum CE of ~98.7 was obtained at $1\,mA\,cm^{-2}$ and the CE decreased at current rates above or below $1\,mA\,cm^{-2}$. The decrease in CE at lower current density could be due to the increase in side reactions, because the activation energy barrier for side reaction decreases with current density and metal deposition occurs more slowly. By contrast, with increasing current density, more inactive lithium byproducts could be formed, because the inactive lithium metal trapped in the carbonaceous fibers can become more concentrated as the kinetic barrier increases. However, the average CE of the CNHs, which ranged from ~97.3% to 98.7% in a wide current density range, is noteworthy. The high CE is further increased by doping with sulfur atoms. The average CE of the S-CNHs is

~99.3% at $1\,mA\,cm^{-2}$ and it decreases to ~98.8 and ~98.6% at lower and higher current densities, respectively. The improved CE of the S-CNHs is closely related to the enhanced chemical stability originating from sulfur doping. As shown in Figure 3A, the ex situ XPS C 1s depth profile of the CNHs after the 110th cycle reveals that their carbon structure is fully passivated with oxygen groups such as C-O and $Li_2CO_3$. The O 1s spectrum also shows a large increase in C-O, $Li_2CO_3$, and Li-O functional groups, indicating large numbers of side reactions and byproducts (Figure 3B). By contrast, the ex situ XPS C 1s depth profile of the S-CNHs shows primarily the $sp^2$-hybridized carbon bond, although the C-O and $Li_2CO_3$ bonds are slightly higher after the 110th cycle (Figure 3C). Moreover, the Li-O-to-C-O bond intensity
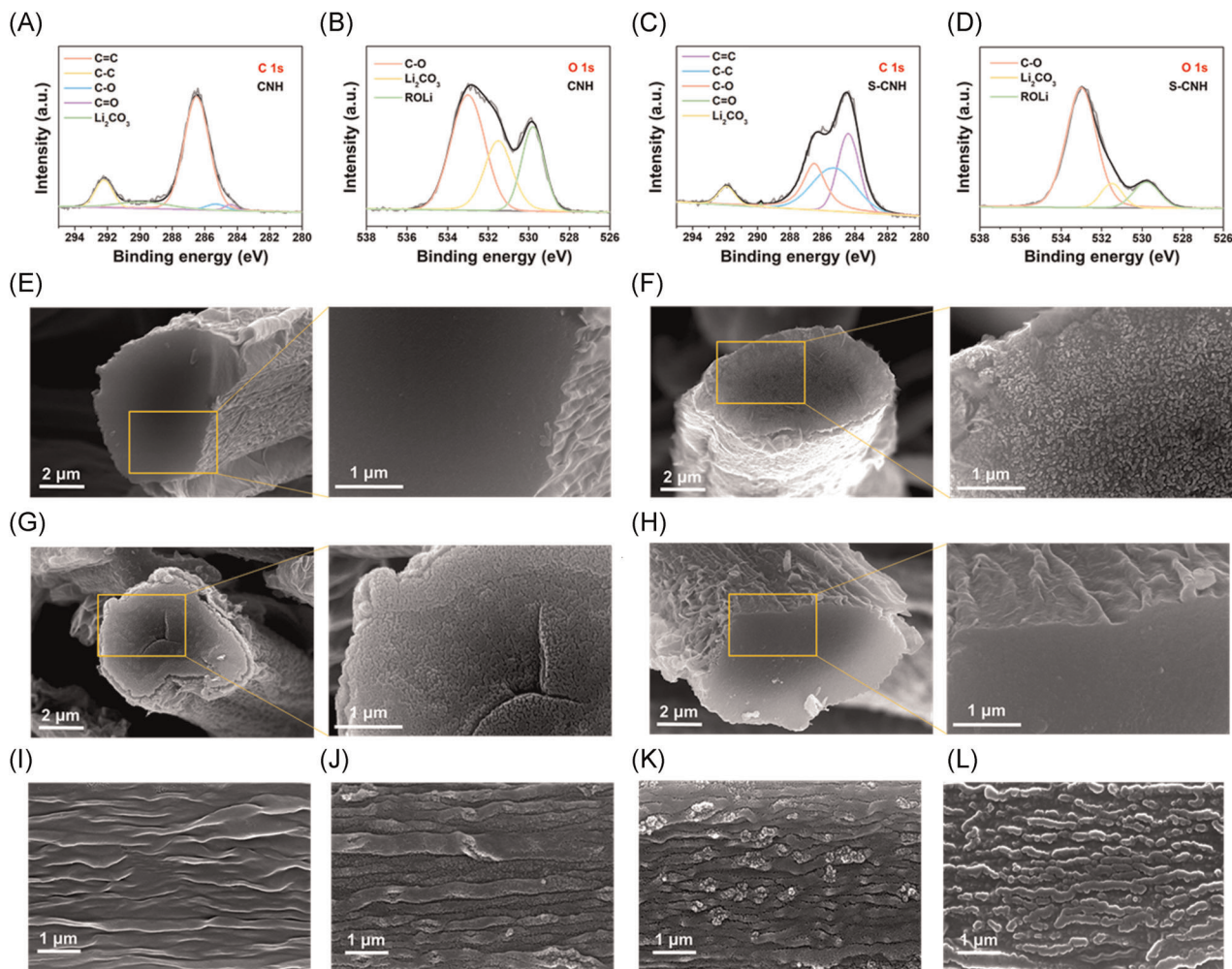
**FIGURE 3** Ex situ analysis results. Ex situ XPS (A) C 1s and (b) O 1s depth profiles of CNH electrode and (C) C 1s and (D) O 1s depth profiles of S-CNH electrode after 110th cycle and Ar etching for 100 s; (E) cross-sectional FE-SEM images of a S-CNH fiber at different magnifications; ex situ cross-sectional FE-SEM images of S-CNH fibers at different magnifications after lithium metal deposition at (F) 3 mAh cm$^{-2}$ and (G) 5 mAh cm$^{-2}$ and (H) after lithium metal dissolution from (F); (I) FE-SEM image of lateral morphology of a S-CNH fiber; ex situ FE-SEM images after lithium metal deposition at (J) 3, (K) 5, and (L) 10 mAh cm$^{-2}$. CNH, carbon-based nanoporous host; FE-SEM, field emission scanning electron microscopy; S-CNH, sulfur-doped carbon-based nanoporous host; XPS, X-ray photoelectron spectroscopy

ratio is much lower than that of the CNHs, indicating that the formation reaction of inactive lithium by-products was retarded by sulfur doping (Figure 3D). The better chemical stability originating from sulfur doping resulted in significantly improved cycling performance (Figure 2G). In continuous galvanostatic lithium metal deposition/dissolution cycling tests with a cut-off capacity of 5 mAh cm$^{-2}$ at an areal current density of 2 mA cm$^{-2}$, the S-CNHs reveal highly stable cycling behavior over ~600 cycles, which is four times longer than the number of stable cycle (~150) achieved with CNHs under the same conditions. During long-term cycling, the S-CNHs reached a high CE of ~99.4%, indicating their practicability. To further investigate the cycling performance, symmetric cell tests of both the CNHs and S-CNHs were conducted at a current density of 2 mA cm$^{-2}$

(Figure 2H). Two electrodes of the same type (CNH// CNH or S-CNH//S-CNH), including lithium metal of 5 mAh cm$^{-2}$, were used for the symmetric cell tests. As shown in Figure 2F, the cycle number versus voltage profiles confirm the highly stable cycling behavior of S-CNHs; the initial LMNO values were maintained over 600 cycles with no fluctuation, and the cycle life of the S-CNH//S-CNH cells was twice that of the CNH//CNH cells.

The effects of nanopores on the lithium metal storage behavior of the S-CNH electrodes were investigated using ex situ FE-SEM characterization (Figures 3E–L). Cross-sectional FE-SEM images of a pristine S-CNH fiber at different magnifications show a smooth fracture surface with no topological features (Figure 3E). After lithium metal deposition at 3 mAh cm$^{-2}$, numerous

nanoparticles with tens of nanometers in width appear homogeneously on the entire fracture surface of an S-CNH fiber (Figure 3F). As more lithium metal is deposited at $5 \, mAh \, cm^{-2}$, the fracture surface is densely filled with more nanoparticles (Figure 3G). The densely packed lithium metal was fully removed by the stripping process and the initial smooth surface was recovered (Figure 3H). These ex situ FE-SEM observations demonstrate that lithium metal is reversibly deposited in the internal nanopores of the fibrous S-CNH electrode as well-distributed lithium nanoparticles. In addition, ex situ FE-SEM images of the S-CNH fibers in the axial direction reveal lithium metal deposition capacities of 3, 5, and $10 \, mAhcm^{-2}$ (Figures 3I–L). In $3 \, mAh \, cm^{-2}$ deposition, the lateral surface of the S-CNH fibers is homogeneously covered by abundant small lithium nanoparticles, and the initial morphological characteristics of flattened nanofibrous patterns are maintained (Figures 3I,j). The nanoparticles are partially agglomerated as more lithium metal is deposited at $5 \, mAhcm^{-2}$ and are enlarged according to the nanofibrous patterns with further lithium metal deposition at $10 \, mAh \, cm^{-2}$, indicating that the S-CNH electrodes have a high capacity for lithium metal accommodation. The similar lithium metal storage behaviors in the internal nanopores were observed on the ex situ FE-SEM images of CNH fibers, where lithium metals were homogeneously deposited in the entire areas of the fractured surfaces and the fiber surfaces (Figure S7). This result supports our claim that the clear difference in the cycling stability, as

shown in Figure 2G,H, originates from the chemical stability. After a long-term cycling process, the nanopores are clogged with byproducts, which can induce an abrupt cycling dead (Figure S8). Nevertheless, the S-CNH-based protective lithium metal deposition/dissoluton cycles can endure more than ~600 cycles, as shown in Figure 2G,H, which demonstrates a practicability of the sulfur-doped nanopore-guided LMA strategy. The schematic image shown in Figure S9 depicts the S-CNH-guided deposition of protective lithium metal on the internal nanopores of the hierarchically bunched carbon nanofibrils.

The feasibility of the S-CNH-based LMA was further investigated by full-cell tests using sulfur copolymer (S-DIB) cathodes composed of sulfur and DIB at a sulfur-to-DIB weight ratio of 4 (Figure S10). As the shuttle effect of the sulfur cathode can be mitigated by the DIB crosslinker, the S-DIB shows a relatively stable cycling performance; thus, it was selected for use with the high-performance LMA.[35,36] S-DIB cathodes with an active loading density of $\sim 5 \, mg \, cm^{-2}$ can deliver a specific capacity of ~950 mAh $g_{cathode}^{-1}$ with an average discharge voltage of ~2.10 V at a current rate of $0.2 \, A \, g^{-1}$ (Figure 4A). These values correspond to a maximum energy density of $\sim 2000 \, W \, h \, kg_{cathode}^{-1}$. The S-CNH-based LMA was prepared after precycling for 10 cycles of lithium metal deposition/dissolution, where $5 \, mAh \, cm^{-2}$ of lithium metal was deposited in the S-CNH electrode. The precycled Li/S-CNH anode was assembled with the S-DIB cathode at an N/P ratio of 1.05, where the Li/S-CNH anode of $\sim 5 \, mg \, cm^{-2}$ ($\sim 1.3 \, mg \, cm^{-2} \, Li + \sim 3.7 \, mg \, cm^{-2}$ S-CNH) corresponding to
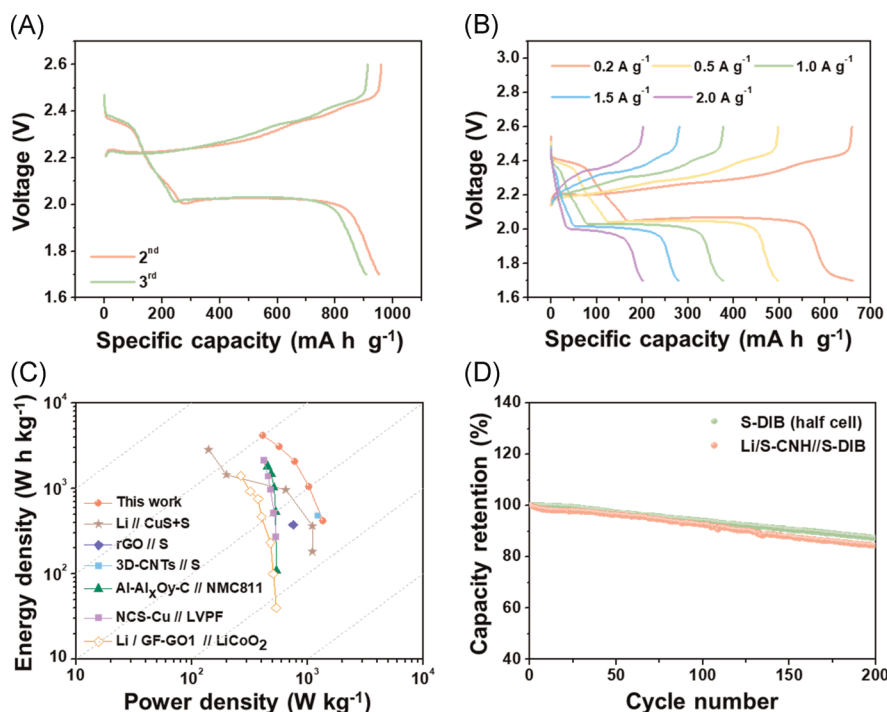


**FIGURE 4** Electrochemical performance of S-DIB cathode and Li/S-CNH//S-DIB full cells in a voltage range of 1.7–2.6 V. Galvanostatic charge/discharge profiles of (A) S-DIB cathode at $0.2 \, A \, g_{cathode}^{-1}$ and (B) Li/S-CNH//S-DIB full cells at different current rates; (C) Ragone plots of several lithium metal batteries including Li/S-CNH//S-DIB full cells; (D) cycling performance of Li/S-CNH//S-DIB full cells and S-DIB cathode (half-cell) at $0.5 \, A \, g_{electrode}^{-1}$ over 200 cycles. S-CNH, sulfur-doped carbon-based nanoporous host; S-DIB, 1,3-diisopropenylbenzene

~3860 mAh $g_{lithium}^{-1}$ (~1000 mAh $g_{lithium + S-CNH}^{-1}$) was used for the full-cell test. As the S-CNH is used as a substrate instead of a typical Cu foil, the specific capacities and current densities of the full cells were calculated by using the mass of both active S-DIB and lithium metal (unit: mAh $g_{electrode}^{-1}$).

Galvanostatic charge/discharge profiles of the Li/S-CNH//S-DIB full cells reveal a reversible capacity of ~660 mAh$g_{electrode}^{-1}$ and an average voltage of ~2.08 V at a current rate of 0.2 A $g_{electrode}^{-1}$ (Figure 4B). As the current rate was increased to 0.5, 1.0, 1.5, and 2.0 A $g_{electrode}^{-1}$, the reversible capacity gradually decreased to ~500, ~380, ~280, and ~200 mAh $g_{electrode}^{-1}$, with an average voltage of ~2.08, ~2.06, ~2.06, and ~2.06 V, respectively. In the full-cell tests, the specific current densities of 0.2, 0.5, 1.0, 1.5, and 2.0 A $g^{-1}$ can be converted into the areal current densities of 1.26, 3.15, 6.30, 9.45, and 12.60 mA $cm^{-2}$, respectively. In the areal current densities between 1.26 and 6.30 mA $cm^{-2}$, as shown in Figure S11a–c, average CE values of the Li/S-CNH anode are similar to the half-cell results in the current densities between 1.0 and 6.0 mA $cm^{-2}$ (Figure 2F). When the areal current densities were higher than 9.45 and 12.60 mA $cm^{-2}$, average CE values were decreased by 98.5% and 98.3%, respectively (Figure S11d,e). Although the average CE values are decreased with areal current rates, the 98.3% is still high, indicating that the critical capacity decay in the full cells, as shown in Figure 4B, did not originate from the Li/S-CNH anode. The maximum energy density of the Li/S-CNH//S-DIB full cells was calculated as ~1370 W h $kg_{electrode}^{-1}$ at ~420 W $kg_{electrode}^{-1}$, and their power density reached 4120 W $kg_{electrode}^{-1}$ at ~410 W h $kg_{electrode}^{-1}$. The energy–power relationship is represented more clearly in Ragone plots, which are presented in Figure 4C, and these of previously reported lithium metal batteries are also provided for comparison.[37–42] The Ragone plots demonstrate that the Li/S-CNH//S-DIB full cells have the highest energy and power densities among all the lithium metal batteries. Moreover, the Li/S-CNH//S-DIB full cells showed superb cycling stability over 200 cycles, where ~85% of the initial capacity was maintained (Figure 4D). The capacity retention of the Li/S-CNH//S-DIB full cells with cycles is similar to that of S-DIB cahthode in a half-cell test (Figure 4D), indicating that the continuous capacity decay originates from the S-DIB cathode rather than the Li/S-CNH anode. Hence, the cycling performance data demonstrate the practicability of S-CNH-based Li–S batteries.

## 4 | CONCLUSION

CNHs and S-CNHs, which are similar except for the presence or absence of sulfur, were prepared to examine the effects of nanopores and sulfur doping. Sulfur doping of CNH electrode materials results in a decrease in the LMNO,

an increase in the average CE in a wide range of current densities, and more stable cycling performance. Moreover, it was observed that nanopores can act as hosts and accommodate lithium metal. In the homogeneously distributed nanopores in the S-CNH fibers, lithium metal nanoparticles were uniformly grown and reversibly removed by a stripping process. The synergistic effects of the nanopores and sulfur doping on the CNH electrode result in a high average CE of ~99.4% in a wide range of current densities and stable cycling over 600 cycles. In addition, the feasibility of S-CNH-based LMAs was demonstrated in full-cell Li–S battery tests with a S-DIB cathode. The Li/S-CNH//S-DIB full cells exhibited a high energy density of ~1370 W h $kg_{electrode}^{-1}$ at ~420 W $kg_{electrode}^{-1}$ and a high power density of 4120 W $kg_{electrode}^{-1}$ at ~410 W h $kg_{electrode}^{-1}$. Moreover, the capacity retention was 85% after 200 stable cycles.

## ORCID
Young Soo Yun https://orcid.org/0000-0002-9643-596X

## REFERENCES
1. Bruce PG, Freunberger SA, Hardwick LJ, Tarascon JM. Li-O$_2$ and Li-S batteries with high energy storage. *Nat Mater*. 2012;11(1): 19-29.
2. Xu W, Wang J, Ding F, et al. Lithium metal anodes for rechargeable batteries. *Energy Environ Sci*. 2014;7(2): 513-537.
3. Pathak R, Chen K, Gurung A, et al. Fluorinated hybrid solid-electrolyte-interphase for dendrite-free lithium deposition. *Nat Commun*. 2020;11(1):93.
4. Jin S, Ye Y, Niu Y, et al. Solid-solution-based metal alloy phase for highly reversible lithium metal anode. *J Am Chem Soc*. 2020;142(19):8818-8826.
5. Liu Y, Lin D, Liang Z, Zhao J, Yan K, Cui Y. Lithium-coated polymeric matrix as a minimum volume-change and dendrite-free lithium metal anode. *Nat Commun*. 2016;7:10992.
6. Kalyani P, Chitra S, Mohan T, Gopukumar S. Lithium metal rechargeable cells using Li$_2$MnO$_3$ as the positive electrode. *J Power Sources*. 1999;80(1-2):103-106.
7. Yamajaki J-I, Tobishima S-I, Sakurai Y, Saito K-I, Hayashi K. Safety evaluation of rechargeable cells with lithium metal anodes and amorphous V$_2$O$_5$ cathodes. *J Appl Electrochem*. 1998;28:135-140.
8. Shi P, Cheng X-B, Li T, et al. Electrochemical diagram of an ultrathin lithium metal anode in pouch cells. *Adv Mater*. 2019; 9(37):1902785.

9. Chen S, Zhang J, Nie L, et al. All-solid-state batteries with a limited lithium metal anode at room temperature using a garnet-based electrolyte. *Adv Mater*. 2021;33(33):2002325.

10. Yuan S, Weng S, Wang F, et al. Revisiting the designing criteria of advanced solid electrolyte interphase on lithium metal anode under practical condition. *Nano Energy*. 2021;83:105847.

11. Kang T, Wang Y, Guo F, et al. Self-assembled monolayer enables slurry-coating of Li anode. *ACS Cent Sci*. 2019;5(3): 468-476.

12. Fan Y, Niu Z, Zhang F, Zhang R, Zhao Y, Lu G. High-energy lithium metal pouch cells with limited anode swelling and long stable cycles. *Nat Energy*. 2019;4(7):551-559.

13. Shi P, Li T, Zhang R, et al. Lithiophilic $LiC_6$ layers on carbon hosts enabling stable Li metal anode in working batteries. *Adv Mater*. 2019;31(8):1807131.

14. Lin D, Liu Y, Liang Z, et al. Layered reduced graphene oxide with nanoscale interlayer gaps as a stable host for lithium metal anodes. *Nat Nanotechnol*. 2016;11(7):626-632.

15. Liu Y, Zhen Y, Li T, et al. High-capacity, dendrite-free, and ultrahigh-rate lithium-metal anodes based on monodisperse N-doped hollow carbon nanospheres. *Small*. 2020;16(44): 2004770.

16. Zhang R, Cheng X-B, Zhao CZ, et al. Conductive nanostructured scaffolds render low local current density to inhibit lithium dendrite growth. *Adv Mater*. 2016;28(11):2155-2162.

17. Zhou T, Shen J, Wang Z, et al. Regulating lithium nucleation and deposition via MOF-derived Co@C-modified carbon cloth for stable Li metal anode. *Adv Funct Mater*. 2020;30(14): 1909159.

18. Ye H, Xin S, Yin YX, Li JY, Guo YG, Wan LJ. Stable Li plating/stripping electrochemistry realized by a hybrid Li reservoir in spherical carbon granules with 3D conducting skeletons. *J Am Chem Soc*. 2017;139(16):5916-5922.

19. Ha S, Hyun JC, Kwak JH, Lim H-D, Yun YS. Hierarchically nanoporous 3D assembly composed of functionalized onion-like graphitic carbon nanospheres for anode-minimized Li metal batteries. *Small*. 2020;16(39):2003918.

20. Wang H, Lin D, Xie J, et al. An interconnected channel-like framework as host for lithium metal composite anodes. *Adv Energy Mater*. 2019;9(7):1802720.

21. Lin D, Liu Y, Cui Y. Reviving the lithium metal anode for high-energy batteries. *Nat Nanotechnol*. 2017;12(3):194-206.

22. Park S, Jin H-J, Yun YS. Advances in the design of 3D-structured electrode materials for lithium-metal anodes. *Adv Mater*. 2020;32(51):2002193.

23. Wen Z, Li H, Liu J, Yang Y, Zhao J. Self-standing N-doped carbonized cellulose fiber as a dual-functional host for lithium metal anodes. *ACS sustainable Chem Eng*. 2021;9(5): 2326-2337.

24. Chen L, Chen H, Wang Z, et al. Self-supporting lithiophilic N-doped carbon rod array for dendrite-free lithium metal anode. *Chem Eng J*. 2019;363:270-277.

25. Lee ME, Kwak HW, Kwak JH, Jin H-J, Yun YS. Catalytic pyroprotein seed layers for sodium metal anodes. *ACS Appl Mater Interfaces*. 2019;11(13):12401-12407.

26. Ma J-l, Meng F-l, Yu Y, et al. Prevention of dendrite growth and volume expansion to give high-performance aprotic bimetallic Li-Na alloy-$O_2$ batteries. *Nat Chem*. 2019;11:64-70.

27. Hao F, Verma A, Mukherjee PP. Mechanistic insight into dendrite-SEI interactions for lithium metal electrodes. *J Mater Chem A*. 2018;6(40):19664-19671.

28. Liu Y, Xue JS, Zheng Y, Dahn JR. Mechanism of lithium insertion in hard carbons prepared by pyrolysis of epoxy resins. *Carbon*. 1996;34(2):193-200.

29. Cho SY, Yun YS, Lee S, et al. Carbonization of a stable β-sheet-rich silk protein into a pseudographitic pyroprotein. *Nat Commun*. 2015;6:7145.

30. Cho SY, Yun YS, Jang D, et al. Ultra strong pyroprotein fibres with long-range ordering. *Nat Commun*. 2017;8:74.

31. Lee ME, Lee S, Choi J, Jin H-J, Han S, Yun YS. Anode-free sodium metal batteries based on nanohybrid core-shell templates. *Small*. 2019;15(37):1901274.

32. Cui J, Yao S, Ihsan-Ul-Haq M, Wu J, Kim JK. Correlation between Li plating behavior and surface characteristics of carbon matrix toward stable Li metal anodes. *Adv Energy Mater*. 2019;9(1):1802777.

33. Chen X, Chen X-R, Hou T-Z, et al. Lithiophilicity chemistry of heteroatom-doped carbon to guide uniform lithium nucleation in lithium metal anodes. *Sci Adv*. 2019;5(2):eaau7728.

34. Yun YS, Le V-D, Kim H, et al. Effects of sulfur doping on graphene-based nanosheets for use as anode materials in lithium-ion batteries. *J Power Sources*. 2014;262:79-85.

35. Yun YS, Yoon G, Park M, et al. Restoration of thermally reduced graphene oxide by atomic-level selenium doping. *NPG Asia Mater*. 2016;8:e338.

36. Simmonds AG, Griebel JJ, Park J, et al. Inverse vulcanization of elemental sulfur to prepare polymeric electrode materials for Li–S batteries. *ACS Macro Lett*. 2014;3(3):229-232.

37. Chung WJ, Griebel JJ, Kim ET, et al. The use of elemental sulfur as an alternative feedstock for polymeric materials. *Nat Chem*. 2013;5(6):518-524.

38. Patel MD, Cha E, Kang C, Gwalani B, Choi W. High performance rechargeable Li-S batteries using binder-free large sulfur-loaded three-dimensional carbon nanotubes. *Carbon*. 2017;118:120-126.

39. Li S, Zhang S, Sun C, et al. Honeycomb inspired lithiophilic scaffold for ultra-stable, high-areal-capacity metallic deposition. *Energy Stor Mater*. 2021;35:378-387.

40. Cao J, Zhang D, Zhang X, Sawangphruk M, Qin J, Liu R. A universal and facile approach to suppress dendrite formation for a Zn and Li metal anode. *J Mater Chem A*. 2020;8(18):9331-9344.

41. Li N, Zhang K, Xie K, et al. Reduced-graphene-oxide-guided directional growth of planar lithium layers. *Adv Mater*. 2019; 32(7):1907079.

42. Li S, Ma Y, Wei B. A lightweight, adhesive, dual-functionalized over-coating interphase toward ultra-stable high-current density lithium metal anodes. *Energy Environ Mater*. 2021;4(1):103-110.

43. Cheng JJ, Liu LF, Ou SW, et al. Sulfur/$Cu_xS$ hybrid material for Li/S primary battery with improved discharge capacity. *Mater Chem Phys*. 2019;224:384-388.

## SUPPORTING INFORMATION

Additional Supporting Information may be found online in the supporting information tab for this article.

## AUTHOR BIOGRAPHIES

Ji In Jung received her B.S. degree in major of Polymer Science Engineering from Inha University (Incheon, South Korea) in 2020. She is a candidate for M.S. under the supervision of Prof. Hyoung-Joon Jin and carrying out researches on the carbon-based electrode materials for next-generation metal batteries.

Hyoung-Joon Jin received his B.S. (1994), M.S. (1966), and Ph.D. (2000) degrees in Inha University (Incheon, South Korea) where he is currently a professor in department of Polymer Science and Engineering. From 2001 to 2003, he was a postdoctoral fellow of Chemical and Biological Engineering at Tufts University (USA), where he started his work on natural polymers. His main research interests are polymer-dervied carbon materials (pyropolymers) for energy storage devices.

Young Soo Yun received his B.S. (2007), M.S. (2010), and Ph.D. (2013) degrees in Inha University (Incheon, South Korea) and is currently an associate professor at KU-KIST Graduate School of Converging Science and Technology in Korea University. His research interests include carbon-based materials for energy storage devices such as supercapacitors, rechargeable batteries, and hybrid capacitors.